# DYNAMICAL EVOLUTION OF A CORONAL STREAMER-FLUX ROPE SYSTEM

## II. *A Self-Consistent Non-Planar Magnetohydrodynamic Simulation*

S. T. WU and W. P. GUO
*Center for Space Plasma and Aeronomic Research and Department of Mechanical and Aerospace Engineering, The University of Alabama in Huntsville, Huntsville, AL 35899, U.S.A.*

MURRAY DRYER
*NOAA – Space Environmental Center and Cooperative Institute for Research in Environmental Sciences (CIRES), University of Colorado, Boulder CO 80303, U.S.A.*

(Received 26 July, 1996; in revised form 4 September, 1996)

**Abstract.** The dynamical response of a helmet streamer to a flux rope escape from the sub-photosphere is examined in a physically self-consistent manner within the approximation of axisymmetric three-dimensional magnetohydrodynamics (i.e., so-called '$2\frac{1}{2}$ D'). In contrast to the previous planar analyses of Paper I (Wu, Guo, and Wang, 1995), the present study shows, with the inclusion of out-of-plane components of magnetic and velocity fields, that the magnetic configuration represents a helical flux rope instead of a planar bubble as shown in Paper I. Because of this more physically-realistic configuration, we are able to examine the dynamical evolution of the helical flux rope's interaction with the helmet streamer. This process leads to the formation of two parts of the solar mass ejection: (i) the expulsion of the helmet dome due to eruption of this flux rope, and (ii) the flux rope's eruption itself. When this two-part feature propagates out to the interplanetary space, it exhibits all the physical characteristics of observed interplanetary magnetic clouds. These numerical simulations also show that the dynamical behavior of the streamer-flux rope system has three distinct states: (i) quasi-equilibrium, (ii) non-equilibrium, and (iii) eruptive state depending on the energy level (twist) of the flux rope.

## 1. Introduction

In the first paper of this series (Wu, Guo, and Wang, 1995, hereafter Paper I), we presented a two-dimensional planar magnetohydrodynamic simulation to investigate the dynamical evolution of a coronal helmet streamer due to emerging flux in the form of a magnetic bubble, namely, a detached magnetic structure that has been introduced into the closed region of the streamer. The dynamical behavior of this magnetic structure is determined by the interaction of the three forces, (i.e., magnetic force, gravity and thermal pressure gradient) (see Figures 8–9 of Paper I). The numerical simulation shows three distinct states according to the strength of this detached structure. These three distinct states are: (i) equilibrium, (ii) non-equilibrium, and (iii) eruptive states; these states enable us to understand the physical processes of destabilization of coronal helmet streamers. Recently, Hundhausen (1993) suggested that most observed non-flare associated (loop-like) coronal mass ejections (CMEs) are caused by destabilization of coronal helmet

*Solar Physics* 0: 1–18, 1996.

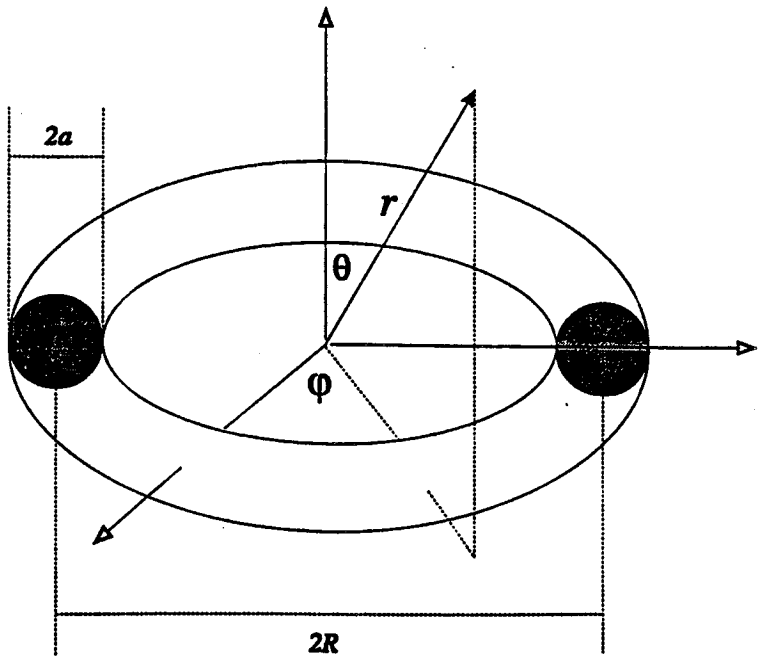


*Figure 1.* Schematic description of the flux-rope's configuration.

streamers. The density features of this and earlier planar MHD simulations did not provide resemblance to the observed loop-like CMEs (Sime, MacQueen, and Hundhausen, 1984). This is, we believe, due to the limitation of the two-dimensional model in which the $B_\phi$ component of the coronal magnetic field, **B**, could not be included. The objective of the present study is to improve this MHD simulation model and, thereby, to enable the results to exhibit typical observed loop-like CMEs. We have extended our previous two-dimensional planar MHD model in pursuit of this objective to the three-dimensional axisymmetrical case (i.e., so-called '$2\frac{1}{2}$-dimensional model'). In this model, the out-of-plane components of the magnetic field and velocity are included; therefore, the magnetic bubble in the planar model becomes a flux rope in the present model as shown in Figure 1.

Recently, a number of authors (Chen and Garren, 1993, Chen 1989; Kumar and Rust, 1996) have investigated the dynamics of the flux rope in the solar/interplanetary space. Because of the importance of flux-rope dynamics as a cause of interplanetary disturbances, such as interplanetary magnetic clouds (Burlaga, Behannon, and Klein, 1987; Lepping, Jones, and Burlaga, 1990), they lead to geomagnetic activity if the Earth is intercepted (Wright and McNamara, 1983; Tsurutani et al. 1988; Gosling et al., 1991, 1994). However, these studies by the above-noted workers are in a form of an analytical approach, thus a complete

MHD description in a self-consistent manner could not be included. In addition, the background of the undisturbed solar-interplanetary atmosphere is treated in an *ad-hoc* basis. In the present study, we will present a self-consistent MHD model in $2\frac{1}{2}$ D with a background atmosphere that has a helmet streamer and a flux-rope under the helmet dome. Then, we will watch this system evolve dynamically on the basis of MHD theory. Section 2 presents the mathematical model and procedures to construct the helmet-streamer and flux-rope system. The numerical results are included in Section 3. Physical interpretations and concluding remarks are given in Section 4.

## 2. Mathematical Model and Method of Treatment

### 2.1. MATHEMATICAL MODEL

The basic equations appropriate to the present study are in the system of spherical coordinates $(r, \theta, \varphi)$, where $r$ is the radius, $\theta$ the co-latitude, and $\varphi$ the longitude with the assumption of axisymmetry (i.e., $\partial/\partial\varphi = 0$). Thus, the equations of mass, momentum, and energy conservation, together with the induction equation, in the ideal MHD approximation are as follows:

$$
\begin{aligned}
\frac{\partial \rho}{\partial t} &= -\frac{1}{r^2}\frac{\partial}{\partial r}(r^2 \rho u_r) - \frac{1}{r\sin\theta}\frac{\partial}{\partial \theta}(\sin\theta \rho u_\theta)\,, \\
\frac{\partial u_r}{\partial t} &= -u_r\frac{\partial u_r}{\partial r} - \frac{u_\theta}{r}\frac{\partial u_r}{\partial \theta} - \frac{1}{\rho}\frac{\partial p}{\partial r} - \frac{1}{r}\left[\frac{\partial}{\partial r}(rB_\theta) - \frac{\partial B_r}{\partial \theta}\right]\frac{B_\theta}{\mu_0 \rho} - \\
&\quad -\frac{1}{r}\frac{\partial}{\partial r}(rB_\varphi)\frac{B_\varphi}{\mu_0\rho} - \frac{GM_s}{r^2} + \frac{u_\theta^2 + u_\varphi^2}{r}\,, \\
\frac{\partial u_\theta}{\partial t} &= -u_r\frac{\partial u_\theta}{\partial r} - \frac{u_\theta}{r}\frac{\partial u_\theta}{\partial \theta} - \frac{1}{\rho r}\frac{\partial p}{\partial \theta} + \frac{1}{r}\left[\frac{\partial}{\partial r}(rB_\theta) - \frac{\partial B_r}{\partial \theta}\right]\frac{B_r}{\mu_0\rho} - \\
&\quad -\frac{1}{r\sin\theta}\frac{\partial}{\partial \theta}(\sin\theta B_\varphi)\frac{B_\varphi}{\mu_0\rho} - \frac{u_r u_\theta}{r} + \frac{u_\varphi^2}{r}\cot\theta\,, \\
\frac{\partial u_\varphi}{\partial t} &= -u_r\frac{\partial u_\varphi}{\partial r} - \frac{u_\theta}{r}\frac{\partial u_\varphi}{\partial \theta} + \frac{1}{r\sin\theta}\frac{\partial}{\partial \theta}(\sin\theta B_\varphi)\frac{B_\theta}{\mu_0\rho} + \frac{1}{r}\frac{\partial}{\partial r}(rB_\varphi)\frac{B_r}{\mu_0\rho} - \\
&\quad -\frac{u_r u_\varphi}{r} - \frac{u_\varphi u_\theta}{r}\cot\theta\,, \qquad (1) \\
\frac{\partial B_r}{\partial t} &= \frac{1}{r\sin\theta}\frac{\partial}{\partial \theta}[\sin\theta(u_r B_\theta - u_\theta B_r)]\,, \\
\frac{\partial B_\theta}{\partial t} &= -\frac{1}{r}\frac{\partial}{\partial r}[r(u_r B_\theta - u_\theta B_r)]\,,
\end{aligned}
$$

$$\frac{\partial B_\varphi}{\partial t} = \frac{1}{r}[r(u_\varphi B_r - u_r B_\varphi)] - \frac{1}{r}\frac{\partial}{\partial \theta}(u_\theta B_\varphi - u_\varphi B_\theta) ,$$

$$\frac{\partial T}{\partial t} = -\frac{1}{r^2}\frac{\partial}{\partial r}(r^2 T u_r) - \frac{1}{r\sin\theta}\frac{\partial}{\partial \theta}(T u_\theta \sin\theta) + (2-\gamma)T\times$$

$$\times\left[\frac{1}{r^2}\frac{\partial}{\partial r}(r^2 u_r) + \frac{1}{r\sin\theta}\frac{\partial}{\partial \theta}(u_\theta \sin\theta)\right] .$$

The parameters are: $u_r$ the radial velocity; $u_\theta$ the meridional velocity; $u_\varphi$ the azimuthal velocity; $B_r$, $B_\theta$, and $B_\varphi$ the components of magnetic field; $\gamma$ the polytropic index ($\gamma = 1.05$); $\mu_0$ the magnetic permeability; $G$ the gravitational constant; $M_s$ the solar mass; $p$ the thermal pressure; $\rho$ the density; and $T$ the temperature. The equation of state, $p = 2nkT$, is used with $n$ as number density; and $k$ as the Boltzmann constant.

## 2.2. METHOD OF TREATMENT

The method of treatment used in this paper is similar to that employed in Paper I to which the interested reader is referred for the details. However, the initial state of this study is a helical flux rope in $2\frac{1}{2}$-D nonplanar geometry imbedded in the closed field region (i.e., helmet dome) of a coronal helmet streamer as shown in Figure 2(b) which is in contrast to the streamer-bubble in a 2-D planar configuration used in Paper I. Therefore, the flux rope is approximated by an axisymmetric magnetic toroid solution given by Shafranov (1960). This solution describes an equilibrium magnetic toroid which satisfies the Grad–Shafranov equation in the approximation of small curvature (see Shafranov, 1960, for details). The expressions of this solution for plasma pressure ($p$) and magnetic field (B) in cylindrical coordinates are:

$$p = \frac{1}{4\pi^2 a^2} J_\varphi J_p \left(1 - \frac{4R^2}{a^2}\frac{(r-R)^2 + z^2}{\delta}\right) +$$

$$+\frac{1}{2\pi^2 a^2} J_p\left(J_p + \frac{5}{4}J_\varphi\right)\left(1 - \frac{4R^2}{a^2}\frac{(r-R)^2+z^2}{\delta}\right)\frac{r^2 - R^2 + z^2}{\delta} + p_0 , \quad (2)$$

$$B_r = \sqrt{\frac{\beta_0}{2}}\frac{8R^4 z}{\pi a^2 \delta^2} J_\varphi - \sqrt{\frac{\beta_0}{2}}\frac{R}{2\pi r}\left(J_p + \tfrac{5}{4}J_\varphi\right)\times$$

$$\times\left[\frac{r^2 - R^2 + z^2}{\delta}\left(-\frac{32 r z R^3}{a^2\delta^2}\right) +\right.$$

$$\left.+\frac{4Rz(R+r)}{\delta^2}\left(1 - \frac{4R^2}{a^2}\frac{(r-R)^2+z^2}{\delta}\right)\right] , \quad (3)$$

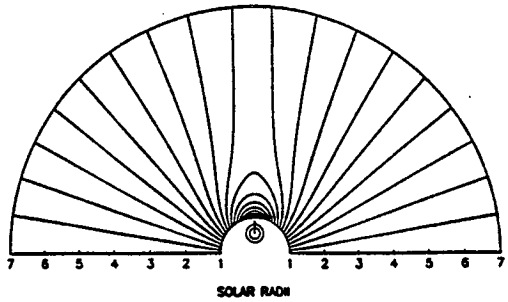


(a)

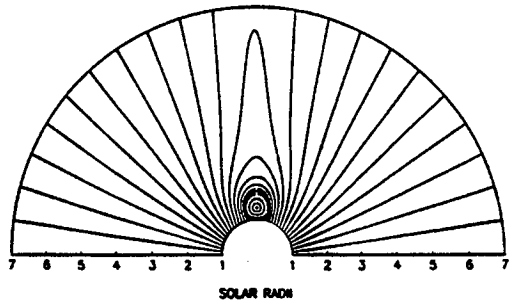


(b)

(c)

*Figure 2.* (a) The initial magnetic field configuration of the helmet streamer and flux-rope. (b) The computed magnetic field configuration of the streamer and flux-rope system after the flux-rope emerged into the closed field region of the streamer for Case 1. (c) The schematic description of the three-dimensional view of the streamer arcade system with a filament in it.

$$B_z = -\sqrt{\frac{\beta_0}{2}}\frac{4R^4(r^2-R^2-z^2)}{\pi a^2 r\delta^2}J_\varphi + \sqrt{\frac{\beta_0}{2}}\frac{R}{2\pi r}(J_p+\tfrac{5}{4}J_\varphi)\times$$
$$\times\left[\frac{(r^2-R^2)^2-z^4}{\delta}\left(-\frac{16R^3}{a^2\delta^2}\right)+\right.$$
$$\left.+\frac{2R(R^2+r^2+2rR-z^2)}{\delta^2}\left(1-\frac{4R^2}{a^2}\frac{(r-R)^2+z^2}{\delta}\right)\right], \qquad (4)$$

$$B_\varphi = \frac{R}{r}\sqrt{\frac{J_\varphi - J_p}{J_p}\beta_0(p-p_0)}, \qquad (5)$$

with

$$\beta_0 = \sqrt{\frac{2\mu_0 p_s}{B_s^2}}, \qquad \delta = (r+R)^2+z^2.$$

$J_\varphi$ and $J_p$ are constants, representing total and partial, current (see Shafranov, 1960, for details). The radius, pressure, magnetic field and currents are normalized, respectively, as follows:

$$R' = r/R_s, \qquad p' = p' = p/p_s,$$
$$B_r' = B_r/B_s, \qquad B_z' = B_z/B_s, \quad B_\varphi' = B_z/B_s, \qquad (6)$$
$$J_\varphi' = J_\varphi\Big/\sqrt{\frac{R_s^2 p_0}{\mu_0}}, \quad J_p' = J_p\Big/\sqrt{\frac{R_s^2 p_0}{\mu_0}},$$

with $R_s$, $p_s$, and $B_s$ being solar radius, plasma pressure, and magnetic field strength on the solar surface, respectively. For convenience, the prime is dropped in Equations (2)–(5) that are the final expressions for an axisymmetric magnetic toroid in cylindrical coordinates. In order to introduce these expressions into the present simulation, we have to transfer them into spherical coordinates $(r, \theta, \varphi)$ as shown in Figure 1 and the parameters to define the flux rope are shown in Table I. For convenience, constants $J_\varphi$ and $J_p$ are replaced by $\beta_1$ and $\beta_2$ which have clearer physical meaning. We set $R = R_s$ in the torus solution, thus, only four parameters remain to determine the solution. It is worth pointing out that Equations (3)–(5) analytically satisfy the solenoidal condition ($\nabla \cdot \mathbf{B} = 0$). In order to assure the numerical accuracy of the solenoidal condition, the divergence-cleaning procedure is again implemented in the present calculation (Ramshwa, 1983) as we did in Paper I.

To proceed with this simulation, we follow the same procedure as described in Paper I by first placing the flux rope below the streamer as shown in Figure 2(a), then allowing the flux rope to move very slowly with respect to the Alfvén speed

Table I
Flux rope parameters

| | |
|---|---|
| $a$ | Flux rope radius |
| $R$ | Large radius (the center of the torus refers to the center of the Sun |
| $p_0$ | Thermal pressure at the surface of the torus |
| $\beta_1$ | plasma $\beta$ at the central axis of the torus |
| $\beta_2$ | plasma $\beta$ at the surface of the torus |

Table II
The three sets of parameters for the description of the flux-rope

| Case | $a$ | $p_0$ | $\beta_1$ | $\beta_2$ |
|---|---|---|---|---|
| 1 | 0.039 $R_s$ | 4.0 $p_s$ | 1.0 | 0.5 |
| 2 | 0.045 $R_s$ | 4.0 $p_s$ | 1.0 | 0.5 |
| 3 | 0.1 $R_s$ | 0.75 $p_s$ | 0.2 | 0.1 |

into the computational domain. The solution that represents the helmet streamer is identical to the one given in Paper I. After the flux-rope moves into the closed field region of the streamer, the numerically relaxed solution for Case I which represent the streamer and flux-rope system is shown in Figure 2(b). On the other two cases, they have similar configuration but are at transient state. These cases can be interpreted as a streamer-arcade with a filament in it, as shown in Figure 2(c).

## 3. Numerical Results

The numerical simulation was carried out for three sets of parameters for the flux-rope (i.e., torus). These three sets (or cases) of parameters are given in Table II.

Using these three sets of representative physical parameters, we again obtained three numerical solutions with distinct states as found in the two-dimensional planar case shown in Paper I. These three distinct states could be classified into three categories; (i) quasi-equilibrium, (ii) non-equilibrium, and (iii) eruptive state. These solutions are shown in Figure 3. The amount of total energy of the flux-rope before entering the streamer in each of these three cases is shown in Table III. It is readily seen from Table III that the eruptive state has the highest total energy content which includes the thermal and magnetic energy. This case is followed by the non-equilibrium and quasi-equilibrium states, respectively. It is also interesting to note from among these three cases, that the magnetic energy increased 75 times from the quasi-equilibrium state to the eruptive state, whereas, the thermal energy increased only by a factor of 16. The latter thermal energy increase is due to the increased mass content in the flux-rope. This comparison indicates that the

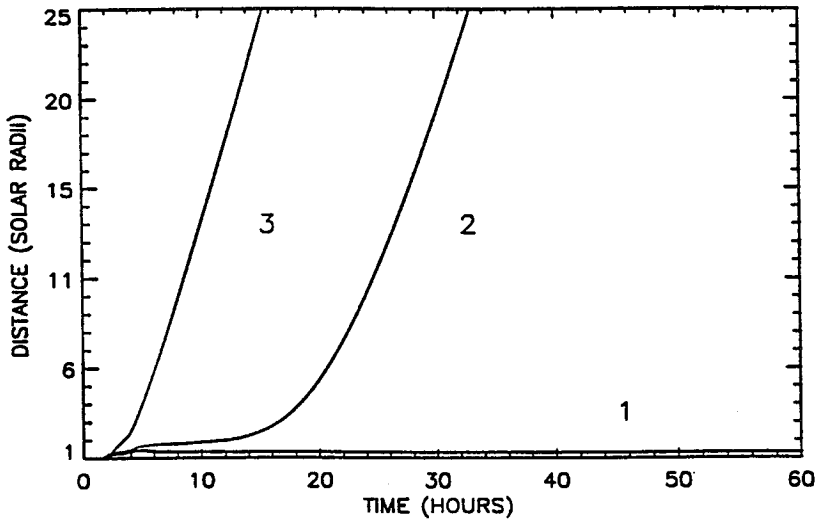


*Figure 3.* Radial distance of the loci of the center of the flux-rope vs time for three cases; (1) quasi-equilibrium state, (2) non-equilibrium state, and (3) eruptive state.

Table III
Energy content of $2\frac{1}{2}$-D magnetic flux-rope (Torus)

| Case | Thermal energy* (ergs) | Magnetic energy* (ergs) |
|---|---|---|
| 1 ($a = 0.039\ R_s$) | $3.61 \times 10^{30}$ | $2.33 \times 10^{29}$ |
| 2 ($a = 0.045\ R_s$) | $4.80 \times 10^{30}$ | $3.10 \times 10^{29}$ |
| 3 ($a = 0.100\ R_s$) | $5.71 \times 10^{31}$ | $1.75 \times 10^{31}$ |

*To compute the energy content, we have assumed the length of the flux rope (i.e., third dimension) as 0.1 $R_s$.

magnetic energy increase may be the primary source and responsible physical agent for the eruption. This can also be seen from an analysis of the interaction of the three forces as shown in Figure 4 and discussed below.

We select the eruptive case (i.e., Case 3) for this discussion to illustrate how this flux-rope destabilizes the helmet streamer to form the CME and its interplanetary consequence (i.e., observed interplanetary magnetic cloud).

### 3.1. INITIATION OF SOLAR MASS EJECTIONS (SME)

As we pointed out in Paper I, the acceleration of the magnetic bubble in the two-dimensional planar case, which may be considered as a flux-rope without twist, is due to the nonlinear interactions of the three major forces (i.e., pressure

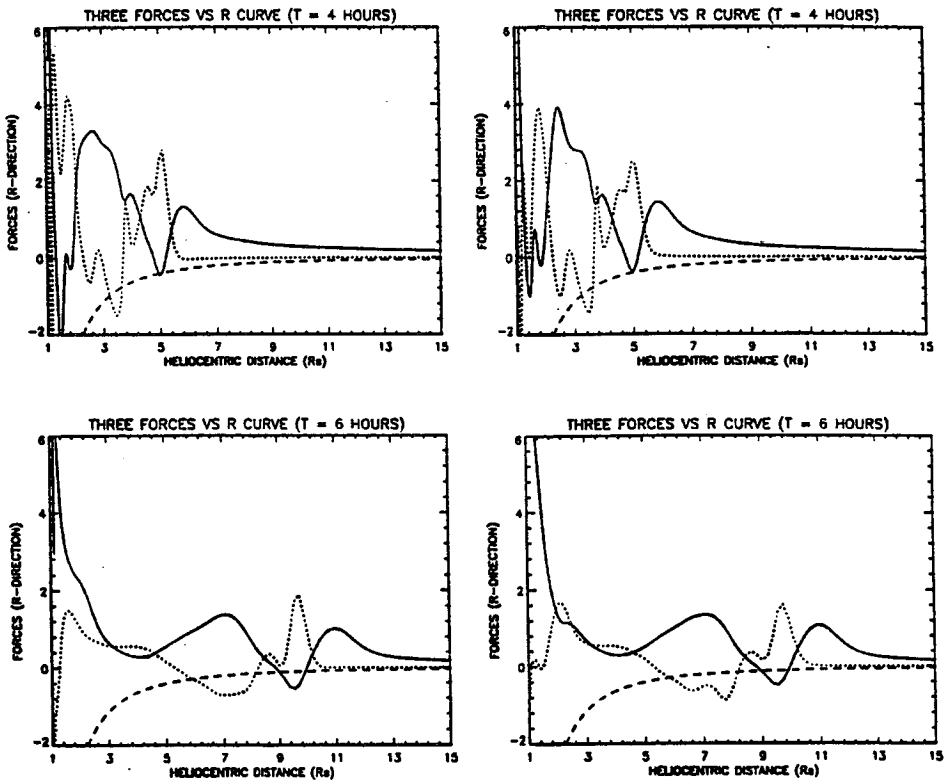


*Figure 4.* Distributions of the pressure gradient force (——), magnetic force (· · · · · ·), and gravitational force (– – –) normalized to the first term of the momentum equation at the equator (left panels) and 5° away from the equator (*right panels*) for time 4 and 6 hours after flux-rope emergence, respectively, for Case 3 (see Table III).

gradient, magnetic, and gravitational forces). Figure 4 shows these three major force distributions at the equator and five degrees off the equator in the left and right panels, respectively, four hours and six hours after the emergence of the flux-rope into the solar atmosphere for Case 3. Figure 4 shows that behind the high density loop (represented by the outward most peak of pressure gradient), there is always a peak of magnetic force which can be interpreted as the magnetic force pushing the loop outward, however, closer to the solar surface, there is a complex interplay among the three forces (i.e., magnetic, pressure, and gravitational forces). The loop itself is clearly driven by the outward Lorentz force ($\mathbf{J} \times \mathbf{B}$) which is represented by the dotted line. This result implies that the propagation and acceleration of the flux-rope is magnetically driven.

Figure 5 shows the evolution of magnetic field lines, velocity vectors, and density contours at 2, 3, and 4 hours after the emergence of the flux-rope. Corresponding

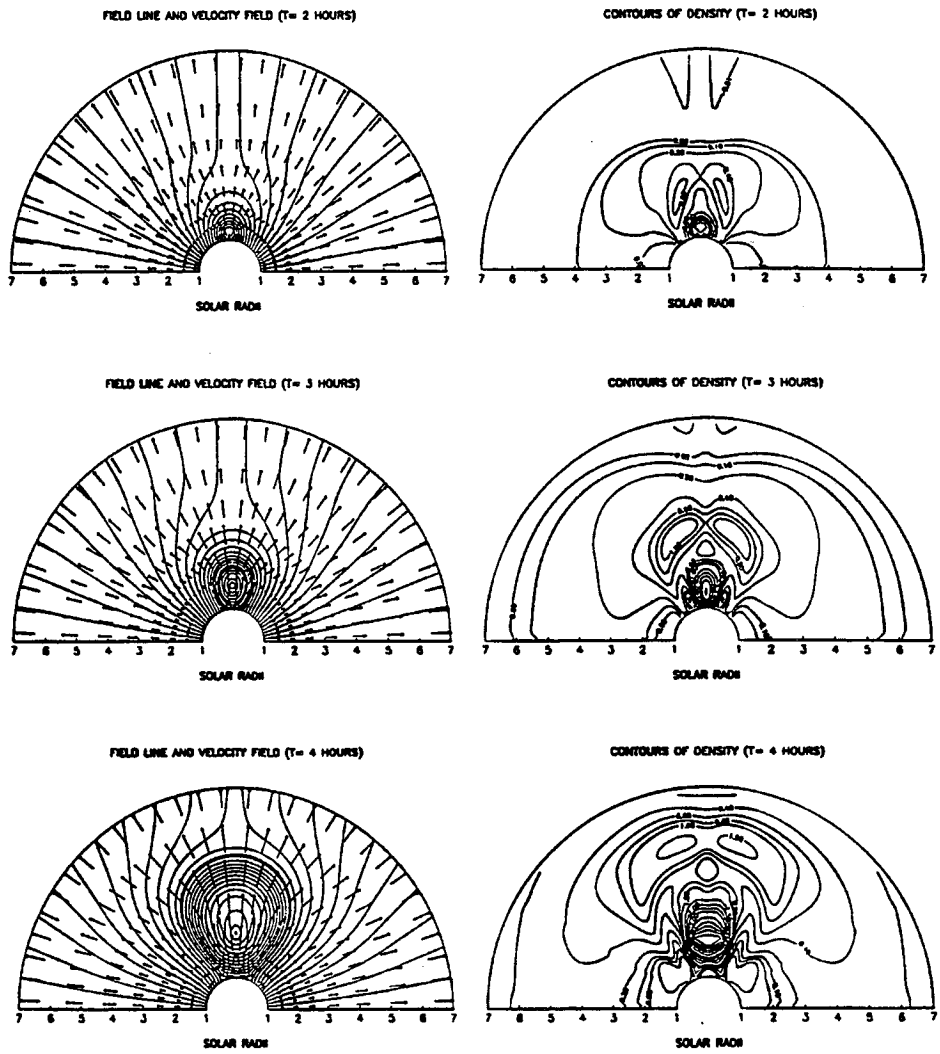


*Figure 5.* The magnetic field lines, velocity vectors, and density contours for Case 3 at $t = 2, 3$, and 4 hours after flux-rope emergence.

plots in a three-dimensional representation are shown in Figure 6 for the magnetic field lines and relative polarization brightness, $pB$. The latter is computed from an integration of the density along the line of sight. From these results, we notice that there are two parts for this solar mass ejection. The first part is due to upward motion of the flux-rope which destabilizes the streamer and, thereby, causes the coronal mass in the helmet dome to form the bright loop of the usually observed

loop-like CMEs (Figures 5 and 6). These results indicate that the greatest density enhancement occurred at the flanks of the loop rather than at the loop apex. This result is similar to the numerical 2D MHD model results given by Steinolfson and Hundhausen (1988) who used a pressure pulse and volumetric heating to generate a CME. The second part of the brightness is caused by the material contained in the flux-rope which may be considered to be the erupted filament. It is worthy to note that the right side panel of Figure 6 shows the 3-D magnetic field configurations of the streamer and flux-rope. At 2 hours, the flux-rope is hidden behind the occulting disk, which is shown as a dark circle. This procedure is necessary for comparisons with coronagraph observations when we need to use the vignetting function for integration of the density along the line of sight in order to present the relative polarization brightness. At the times of 4 and 6 hours, we clearly show the propagation of the flux-rope to interplanetary space, thereby leading to the formation and, presumably, detection of the magnetic cloud. A detailed discussion of this feature is given in the next section.

### 3.2. PROPAGATION OF THE FLUX ROPE

We extended our computation to 30 $R_s$ in order to examine the interplanetary consequences of this streamer and flux-rope system. A grid system of $210 \times 62$ is used for this purpose. Figure 7 shows the magnetic field lines, velocity vectors, and density contours at 8 and 12 hours, respectively, after the emergence of the flux-rope for Case 3 (i.e., eruptive case). Figure 7 is, in fact, the continuation of Figure 6. By examining the evolution of magnetic field lines as shown in Figures 6 and 7, we recognize that the flux-rope has ballooned out, pushing the helmet dome laterally aside, and developing a magnetohydrodynamic fast shock as shown in Figure 8(a). In Figure 8(b) we present the distribution of the MHD fast wave Mach number. Each point on the curve in Figure 8(b) represents the position of the wave front and its corresponding fast wave Mach number at a specific time. This figure shows that the MHD fast shock begins to develop at $\sim 2.5\ R_s$ for this case. This fast MHD shock is caused by the movement of the flux-rope as a piston. It should be noted that in Figure 8(b), the fast wave Mach number does not start at 0. This is because once we start moving the flux rope into the computational domain, it will generate a fast MHD wave. At the very early stage, the real driver, i.e., the flux rope which is expanding slowly, is behind the wave and is not distinguishable. Once the flux rope begins to accelerate, it will generate another wave that will eventually evolve into a fast MHD shock that overtakes the foregoing MHD wave. The radial velocity of the center of the flux-rope is plotted for both the eruptive and non-equilibrium cases as seen in Figure 9. We observe that the radial velocities reach asymptotic values of 420 km $s^{-1}$ and 380 km $s^{-1}$, respectively, for these two cases. The strengths of the azimuthal component of the magnetic field, corresponding to these two values, are 7.24 and 6.32 G, respectively. This means that the shear angle of the twist of

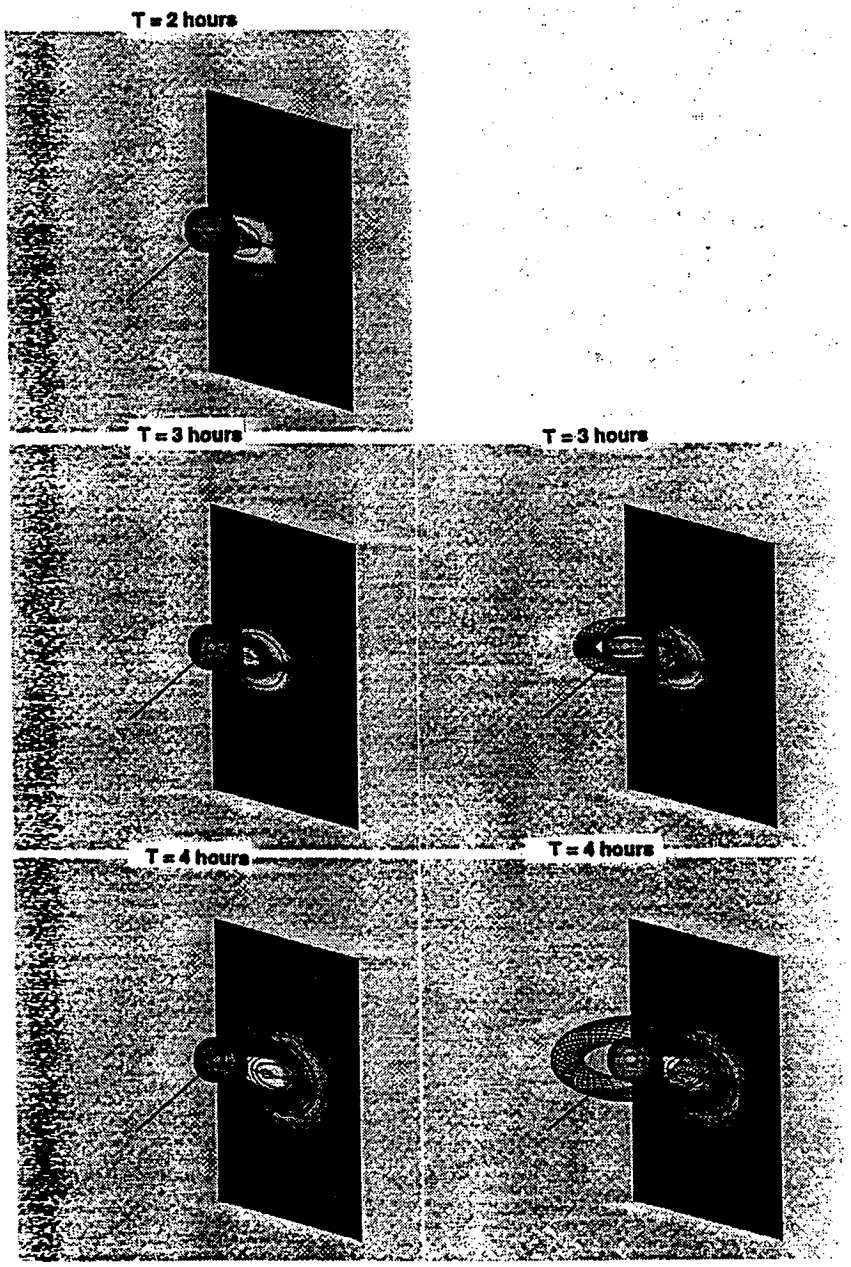


*Figure 6.* Three-dimensional representation of magnetic field lines and relative polarization brightness (pB) in the plane-of-sky for the results given in Figure 5.

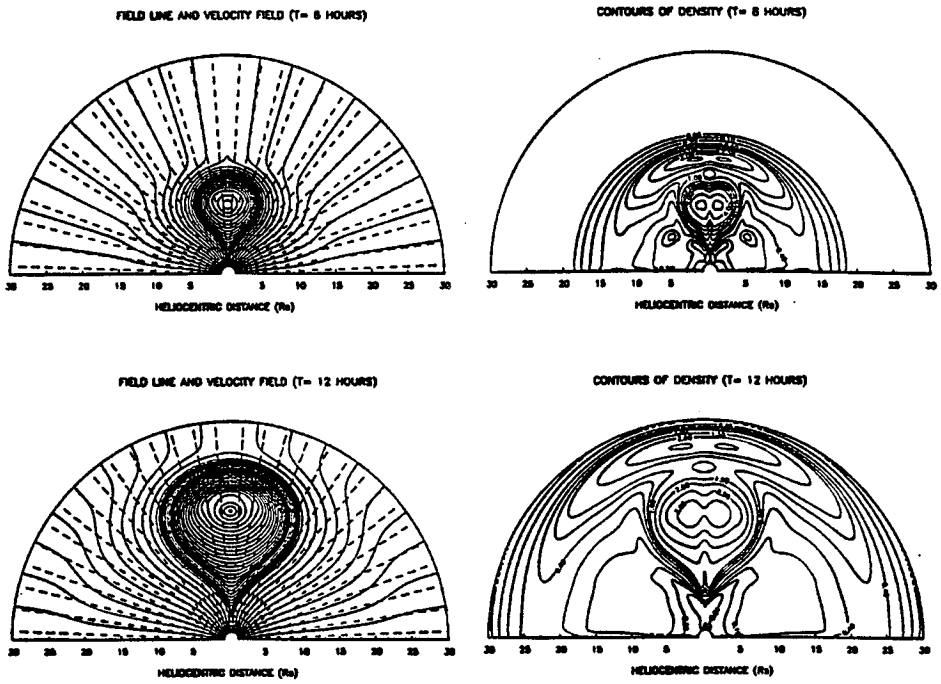


*Figure 7.* The magnetic field lines, velocity vectors, and density contours for Cases 3 at 8 and 12 hours, respectively, after the flux-rope emergence.

the flux rope is the key parameter in the acceleration process for the development of shocks.

Finally we examine the evolution of this streamer flux-rope system in the interplanetary space. We plot, in Figure 10, the density, temperature, radial velocity, and magnetic field as a function of time, at 25 $R_s$ and a displacement of 15° away from the equator for the eruptive case. The magnetic field in Figure 10 is represented in solar ecliptic coordinates in order to compare with observations conveniently at both the hypothetical spacecraft location as well as at larger distances. If we compare Figure 10 with the observations of magnetic clouds at Earth (e.g., Burlaga, Behannon, and Klein, 1987), the local density and temperature minima behind the shock are noted, thereby immediately indicating that they are qualitatively the same. Quantitatively, they are certainly different, because the present results are at 25 $R_s$. We perform several simple extrapolations using the polytropic law. For example, the corresponding temperature minima at 1 AU are: $2.2 \times 10^5$ K for $\gamma = 1.20$; $4.4 \times 10^4$ K for $\gamma = 1.4$; and $0.5 \times 10^4$ K for $\gamma = 1.67$. From these results, we may conclude that when the solar wind expands from the corona to the interplanetary space, additional heating is needed (as expected) for both transient

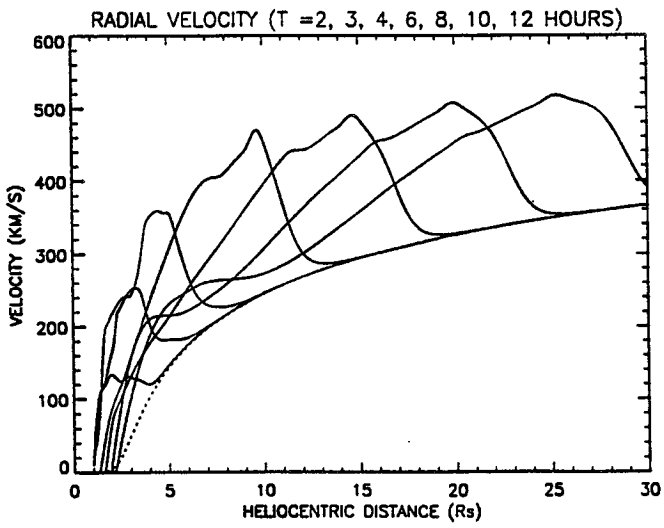


(a)

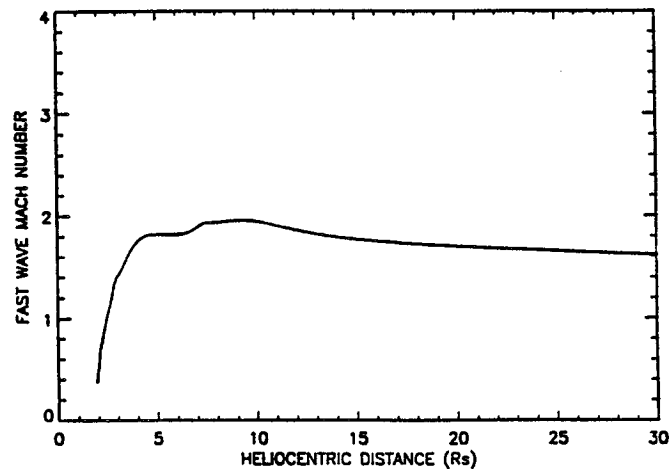


(b)

*Figure 8.* (a) Radial velocity profile at the equator at $t = 2, 3, 4, 6, 8, 10$, and 12 hours for Case 3. (b) Fast MHD wave Mach number distribution at the equator for Case 3.

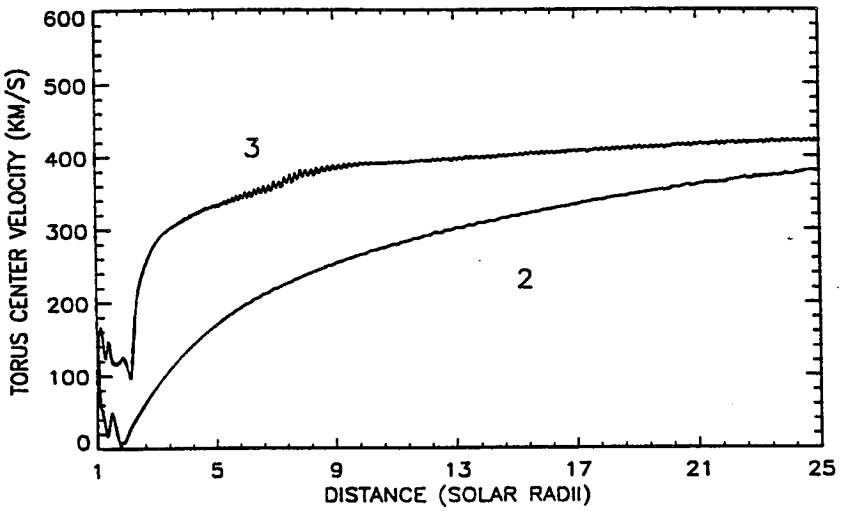


*Figure 9.* The velocity distribution of the flux-rope center for Cases 2 and 3, respectively, corresponding to the non-equilibrium and eruptive cases.

as well as quiescent flows (Suess, Wang, and Wu, 1996). From the density plot of Figure 10, we identify two peaks; the sharp one is the fast MHD shock which is caused by the propagation of the helmet dome, and the fatter one corresponds to the flux-rope. These features are related to our suggestion of solar mass ejections that consist of two parts.

## 4. Physical Interpretations and Concluding Remarks

The self-consistent planar MHD simulation model for the study of the dynamical evolution of a coronal streamer-bubble (Paper I) has now been extended to the nonplanar case (i.e., three-dimensional, axisymmetric geometry). This extension made it possible for us to study the dynamical evolution of a helical structure within a helmet streamer. Physically, this configuration corresponds to a flux-rope emerging from subphotosphere into the helmet dome of a coronal streamer. Thus, we used this model to examine the outward motion of this flux-rope and its interaction with a helmet streamer. The results obtained from this simulation demonstrated, clearly, that there are three distinct states; (i) quasi-equilibrium, (ii) non-equilibrium, and (iii) eruptive state as shown in Figure 3. These three numerical solutions could be interpreted as three different physical states of a flux-rope that may be embedded within the solar atmosphere. If the energy content of the flux-rope (i.e., $B_\varphi$ is small) does not reach a threshold, the energy will remain within the flux-rope in a stationary position for a long time; the consequence is formation

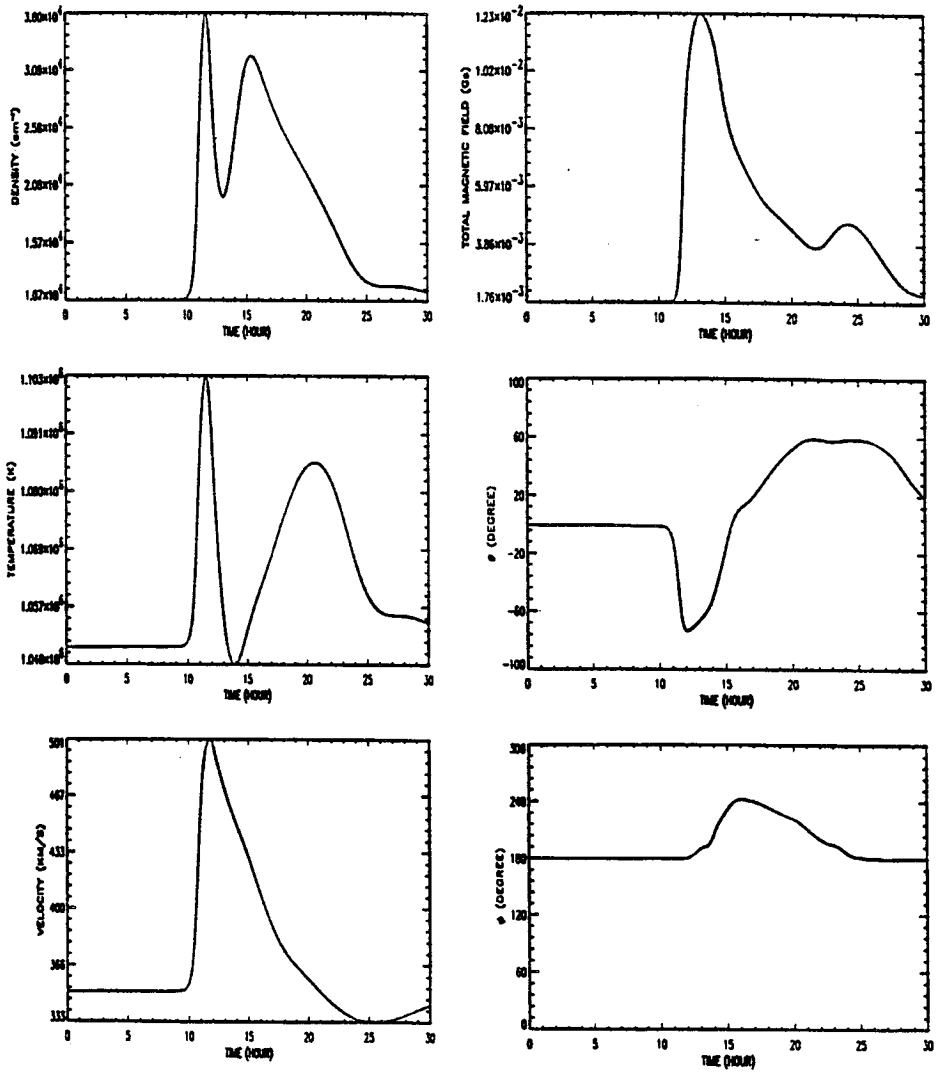


*Figure 10.* The density, temperature, radial velocity, and magnetic field variations versus time at $r = 25\ R_s$ and 15° (away) from the equator for Case 3. The magnetic fields are given in solar ecliptic coordinates (Burlaga, 1988) for direct comparison with a hypothetical spacecraft at that location.

of a stationary filament (i.e., Figure 3, Case 1). If the filament reaches the threshold, its short term future will depend on how far the filament energy content exceeds the threshold. That is, two characteristics are exhibited; one shows a period of a few hours agitation, then outward motion, slowly accelerating over several hours, then

reaching an asymptotic speed propagating outward; the other one is the flux-rope's immediate eruption. These two characteristics are represented by the solutions shown in Figure 3 (i.e., Cases 2 and 3). When this flux-rope takes off, it compresses the helmet dome and pushes it away. These properties are shown in Figures 5 and 6. It is clearly recognized that this eruptive flux-rope has pushed away the coronal mass and magnetic field of the helmet dome to form the bright loop of the typical loop-like CMEs, followed by the mass of the filament that forms the bright core as described in Section 3. When this flux-rope propagates outward, it resembles the magnetic clouds that are sometimes observed in interplanetary space as shown in Figure 10. We have not been able to determine the threshold energy in this limited study because a large number of parametric studies, together with observations, are required. This procedure should be considered when an appropriate data set is available in the future.

In summary, a three-dimensional, axisymmetric, time-dependent, magneto-hydrodynamic model is, for the first time, presented for a self-consistent description of flux-rope emergence from the sub-photosphere. The flux-rope, depending on the amplitude of its magnetic energy content, may either remain in place or be ejected, either immediately or within the time scale of a day. In both of the two latter cases the solar mass ejection consists of two parts: the typically-observed loop-like CME and the mass within the flux rope which could be a bright feature following the loop as shown in this calculation. However, the present results do not possess all the observed features of some global coronal streamer structures that consist of prominence, cavity and helmet dome as pointed out by Low and Hundhausen (1995); the cavity and dense, low temperature prominence are lacking in the present model. We plan to examine this deficiency in the future. On the other hand, we also realize that there are still other physical mechanisms such as photopsheric shearing (Linker and Mikic, 1995) and heating (Wang et al., 1995) that could destabilize the streamer which is worth investigation. To further examine these different scenarios, we should look for observational evidences.

## Acknowledgements

This research efforts were supported by a NASA Grant NAG8W-4665 and NRL through USRA Prime Contract N00014-C-95-2058.

## References

Burlaga, L. F.: 1988, *J. Geophys. Res.* **93**, 7217.
Burlaga, L. F., Behannon, K. W., and Klein, L. W.: 1987, *J. Geophys. Res.* **92**, 5725.
Chen, J.: 1989, *Astrophys. J.* **338**, 453.
Chen, J. and Garren, D. A.: 1993, *Geophys. Res. Letters* **20**, 2319.
Gosling, J. T., McComas, D. J., Phillips, J. L., and Bame, S. J.: 1991, *J. Geophys. Res.* **96**, 7831.

Gosling, J. T., Bame, S. J., McComas, D. J., Phillips, J. L., Goldstein, B. E., and Neugebauer, M.: 1994, *Geophys. Res. Letters* **21**, 1109.
Hundhausen, A. J.: 1993, *J. Geophys. Res.* **98** (A8.13), 177.
Kumar, A. and Rust, D. M.: 1996, *J. Geophys. Res.* **101** (A7), 15667.
Lepping, R. P., Jones, J. A., and Burlaga, L. F.: 1990, *J. Geophys. Res.* **95** (A8), 11957.
Linker, J. A., and Mikic, Z.: 1995, *Astrophys. J.* **438**, L45.
Low, B. C. and Hundhausen, J. R.: 1995, *Astrophys. J.* **443**, 818.
Ramshaw, J. D.: 1983, *J. Comp. Phys.* **52**, 592.
Shafranov, V. D.: 1960, *Soviet Phys. JETP* **37**, 775.
Steinolfson, R. S. and Hundhausen, A. J.: 1988, *J. Geophys. Res.* **93**, 14269.
Sime, D. G., MacQueen, R. M., and Hundhausen, A. J.: 1984, *J. Geophys. Res.* **89**, 2113.
Suess, S. T., Wang, A.-H., and Wu, S. T.: 1996, *J. Geophys. Res.*, ~~in press.~~ 101, A9, 1995
Tsurutani, B. T., Gonzalax, W. D., Tang, F., Akasofu, S. I., and Smith, E.: 1988, *J. Geophys. Res.* **93**, 5437.
Wang, A. H., Wu, S. T., Suess, S. T., and Poletto, G.: 1995, *Solar Phys.* **161**, 365.
Wright, C. S. and McNamara, L. F: 1983, *Solar Phys.* **87**, 401.
Wu, S. T., Guo, W. P., and Wang, J. F.: 199S, *Solar Phys.* **157**, 325 (Paper I).